

BASIS FUNCTIONS FOR TRIANGULAR AND QUADRILATERAL HIGH-ORDER ELEMENTS*T. C. WARBURTON[†], S. J. SHERWIN[‡], AND G. E. KARNIADAKIS[†]

Abstract. In this paper we present a unified description of new spectral bases suitable for high-order hp finite element discretizations on hybrid two-dimensional meshes consisting of triangles and quadrilaterals. All bases presented are for C^0 continuous discretizations and are described both as modal and as mixed modal-nodal expansions. General Jacobi polynomials of mixed weights are employed that accommodate automatic exact numerical quadratures, generalized tensor products, and variable expansion order in each element. The approximation properties of the bases are analyzed in the context of the projection, linear advection, and diffusion operators.

Key words. spectral methods, finite element method, unstructured grids

AMS subject classifications. 35L05, 41A10, 65D15

PII. S1064827597315716

1. Introduction. In spectral methods the question as to what basis functions $\phi_n(x)$ to use to approximate a smooth function $f(x) \approx \sum_{n=0}^N \hat{f}_n \phi_n(x)$ in a separable domain is answered relatively easily. Typically, boundary conditions, fast transforms, and numerical quadrature dictate this choice depending on the particular partial differential equation considered. In multidomain spectral methods which are used in complex-geometry computational domains the choice of the *subdomain shape* is an important factor as well. One can choose arbitrary polygons, for example, to accommodate geometric complexity, but such a choice may prevent the use of polynomial basis functions and lead to prohibitive computational difficulty in maintaining interfacial continuity among subdomains.

Similarly, in the hp version of the finite element method the choice of subdomain shape and associated trial basis ultimately determines the efficiency of the method. Starting with the pioneering work of Szabo in the mid-seventies, several versions of this approach have been formulated for both solid mechanics and fluid dynamics in [1, 2, 3, 4]. Similar formulations were developed to allow greater flexibility in handling geometric complexities and local refinement requirements in [5, 6, 7, 8, 9, 10].

The basis or shape functions employed in the aforementioned formulations typically involve Legendre or Chebyshev one-dimensional polynomials. Multidimensional expansions are constructed using tensor products for quadrilateral or hexahedral elements [11, 12]. A basis directly associated with boundary and interior elemental nodes usually lacks hierarchy, and in addition a variable p -order per element is not readily achievable [3]. However, a *modal* basis can be constructed that consists of vertex modes, edge modes, and interior modes in two dimensions that are hierarchical and allow for a variable order within as well as along the boundary of the element [11]. In addition to the flexibility in more easily handling nonuniform resolution re-

*Received by the editors January 27, 1997; accepted for publication (in revised form) April 22, 1998; published electronically May 6, 1999.

<http://www.siam.org/journals/sisc/20-5/31571.html>

[†]Division of Applied Mathematics, Brown University, Providence, RI 02912 (tcew@cfm.brown.edu, gk@cfm.brown.edu). The work of the third author was sponsored by AFOSR and DOE.

[‡]Department of Aeronautics, Imperial College, South Kensington, London, SW7 2BY, UK (s.sherwin@ic.ac.uk).

quirements, hierarchical bases can lead to better conditioning of mass and stiffness matrices [12], and thus fast iterative algorithms can be effectively employed in the solution algorithms.

The need for constructing p -type bases in triangular domains became evident from the early stage. Peano [13] constructed a hierarchical triangular basis based on area (barycentric) coordinates by selecting as nodal variables high-order tangential derivatives along each side evaluated at the midside and by imposing appropriate continuity constraints for C^0 and C^1 elements. A variation of this construction was later developed [11] that introduces Legendre polynomials to avoid round-off error for high-order p -expansions. However, both approaches require special integration rules which are quite complicated at high polynomial order. Dubiner [14] first developed an alternative hierarchical basis for triangular domains, which unlike Peano's basis is based on Cartesian coordinates and preserves the tensor product property that leads to sum factorization and low operation account, a crucial property for p -type finite elements and spectral methods.

Dubiner's basis was implemented in [15] using a Galerkin formulation of the Navier–Stokes equations, and it was found to be competitive in cost with the nodal basis on quadrilaterals employed in the spectral element method [3]. This new modal basis employs Jacobi polynomials of mixed weight to automatically accommodate exact numerical integration using standard Gauss–Jacobi one-dimensional quadrature rules. In particular, exploiting the tensor product property of the basis, multidimensional integrals can be evaluated efficiently as a series of one-dimensional integrals; similarly the cost of evaluating derivatives or squares of a function is maintained at operation count $\mathcal{O}(N^3)$, where N is the number of modes *per direction* as in the quadrilateral or hexahedral elements.

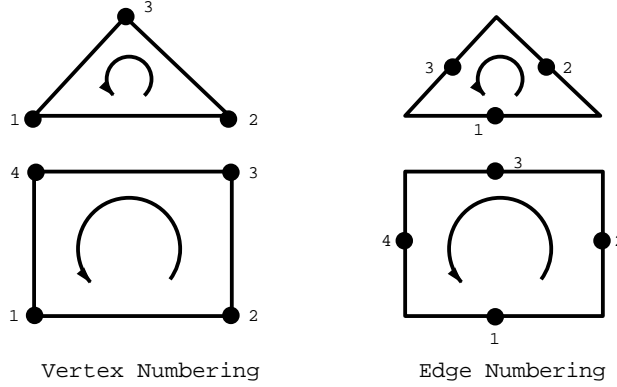
Recent trends in mesh generation have emphasized the use of *hybrid discretizations* consisting of triangular and quadrilateral subdomains in order to provide greater flexibility in refinement and unrefinement procedures. For high-order discretizations this implies that suitable basis functions have to be developed to conform with the subdomain shapes and at the same time preserve the good approximation properties and efficiency of the aforementioned bases. In this work, we develop a unified description of such hybrid basis functions following earlier developments in [14] and [16]. We develop five types of basis functions which are either modal or nodal or mixed and which may or may not be hierarchical.

In section 2 we present the notation and preliminary concepts. In section 3 we present variations of modal bases for triangles and quadrilaterals and in section 4 we do the same for mixed nodal-modal bases. In section 5 we implement the new bases in the context of projection and linear advection and diffusion operators, and in section 6 we conclude with a summary and a comparison of the relative merits of each class of basis functions.

2. Notation and preliminaries.

2.1. Domain definition. We will be considering problems formulated on a domain $\Omega \in R^2$, which is the union of a set of K elemental subdomains (Ω^k). These elemental subdomains may be quadrilaterals or triangles or both. We will approximate a function $f(x, y)$ by a C^0 expansion, over the K subdomains, of the form

$$f(x, y) = \sum_k \sum_n \hat{f}_n^k \phi_n(a(x, y); b(x, y)),$$

FIG. 1. *Vertex and edge numbering of a polygon.*

where \hat{f}_n^k are the expansion coefficients in the k th subdomain and ϕ_n are the basis functions. The coordinates a, b are related to the physical (global) coordinates x, y via appropriate mappings, as will be shown in the following.

A linear element is defined by a set of vertices and edges that are numbered in a counterclockwise manner around the boundary of the element as shown in Figure 1.

2.2. Coordinate system. We wish to introduce three coordinate systems. The first is the Cartesian system (x, y) in which we formulate problems. The second is the (r, s) system, which is a Cartesian coordinate system fitted to the *standard* elements to which we will transform all elements. The last is the (a, b) system, in which we will perform integration and differentiation. We first define the standard triangle as

$$T^2 = \{(r, s) | -1 \leq r, s; r + s \leq 0\}$$

and the standard quadrilateral as

$$Q^2 = \{(a, b) | -1 \leq a, b \leq 1\}.$$

We define a bijection from an arbitrarily oriented straight-sided triangle T^1 to T^2 , $(T_1)^{-1} : T^2 \mapsto T^1$, by

$$\mathbf{x} = -\left(\frac{r+s}{2}\right)\mathbf{x}_1 + \left(\frac{1+r}{2}\right)\mathbf{x}_2 + \left(\frac{1+s}{2}\right)\mathbf{x}_3$$

and a mapping $T_2 : T^2 \mapsto Q^2$ by

$$\begin{aligned} r &= 2\left(\frac{1+a}{2}\right)\left(\frac{1-b}{2}\right) - 1, \\ s &= b. \end{aligned}$$

Clearly we can map between T^1 and Q^2 by composing T^1 and T^2 , as shown in Figure 2.

We also define similar spaces and mappings for the quadrilateral elements. In this case we need to consider only the arbitrary linear quadrilateral Q^1 and the previously defined Q^2 . Similar to mappings between triangles, we define the bijective mapping from Q^1 (arbitrary quadrilateral) to the standard quadrilateral Q^2 by

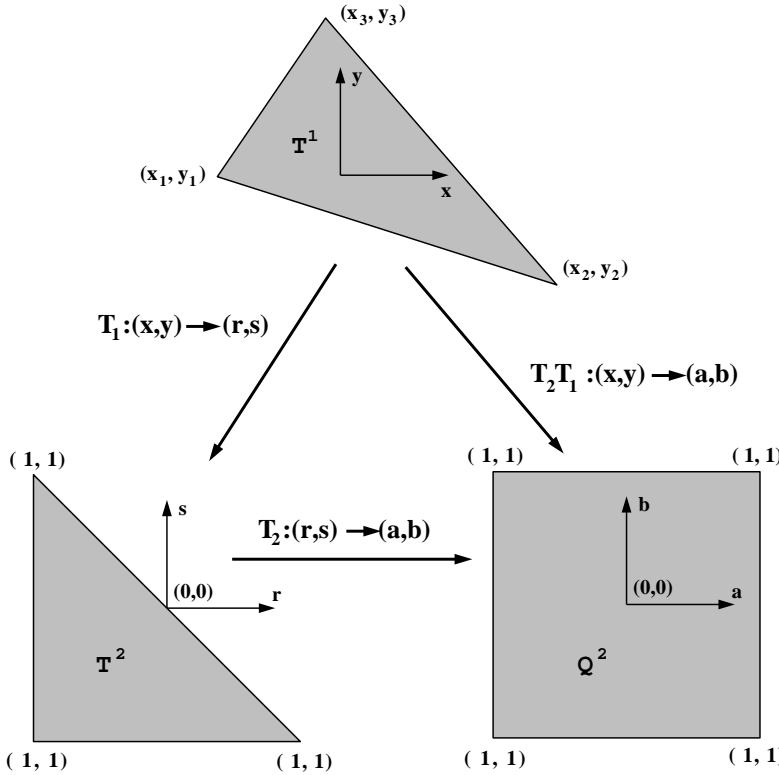


FIG. 2. Transforms between the arbitrary triangle T^1 , standard triangle T^2 , and standard quadrilateral Q^2 .

$$\begin{aligned} \mathbf{x} &= (Q_1)^{-1}(a, b) \\ &= \left(\frac{1-a}{2} \right) \left(\frac{1-b}{2} \right) \mathbf{x}_1 + \left(\frac{1+a}{2} \right) \left(\frac{1-b}{2} \right) \mathbf{x}_2 \\ &\quad + \left(\frac{1+a}{2} \right) \left(\frac{1+b}{2} \right) \mathbf{x}_3 + \left(\frac{1-a}{2} \right) \left(\frac{1+b}{2} \right) \mathbf{x}_4. \end{aligned}$$

2.3. Elemental inner products and transforms. We shall use the notation (f, g) to denote inner product, which in general is defined as

$$(f, g) = \int_{\Omega^k} f(x, y)g(x, y)dxdy$$

or

$$(f, g) = \int_{Q^2} f(x(a, b), y(a, b))g(x(a, b), y(a, b)) \frac{\partial(\mathbf{x}(a, b), \mathbf{y}(a, b))}{\partial(a, b)} dadb.$$

The only difference between the inner product for the triangle and quadrilateral is that the Jacobian of the mapping to the standard quadrilateral is different. Conveniently, this Jacobian can be treated as a constant for linear triangles by choosing the correct integration weights that incorporate its $(1-b)/2$ factor [16]. For the triangle we use Gauss–Lobatto–Legendre (GLL) quadrature in the a directions and Gauss–Radau–Jacobi (GRJ) quadrature in the b direction to perform this integral as

a discrete sum. For the quadrilateral we use GLL quadrature in both the a and the b directions.

Later we will define bases which are products of functions in a and functions in b , so these inner products will degenerate into the product of two one-dimensional integrations. This property will allow us to efficiently evaluate inner products in $O(N^3)$ operations, where N is the expansion order we will be using. We will also use the term polynomial order which is equal to $N - 1$.

2.4. Components of a C^0 basis. We are interested in constructing element-wise approximations to a function. These will be forced to fit together continuously by the choice of basis. The bases we have considered are constructed out of a set of polynomial modes. These modes are delineated into two groups, which we label *boundary modes* and *interior modes*. The interior modes are zero on the element boundary and are similar to the *bubble* modes used in p -type finite elements [11]. The boundary modes themselves are split into two groups: *vertex modes* and *edge modes*. The edge modes are zero at all the vertices and all but one edge. The vertex modes are zero at all but one vertex.

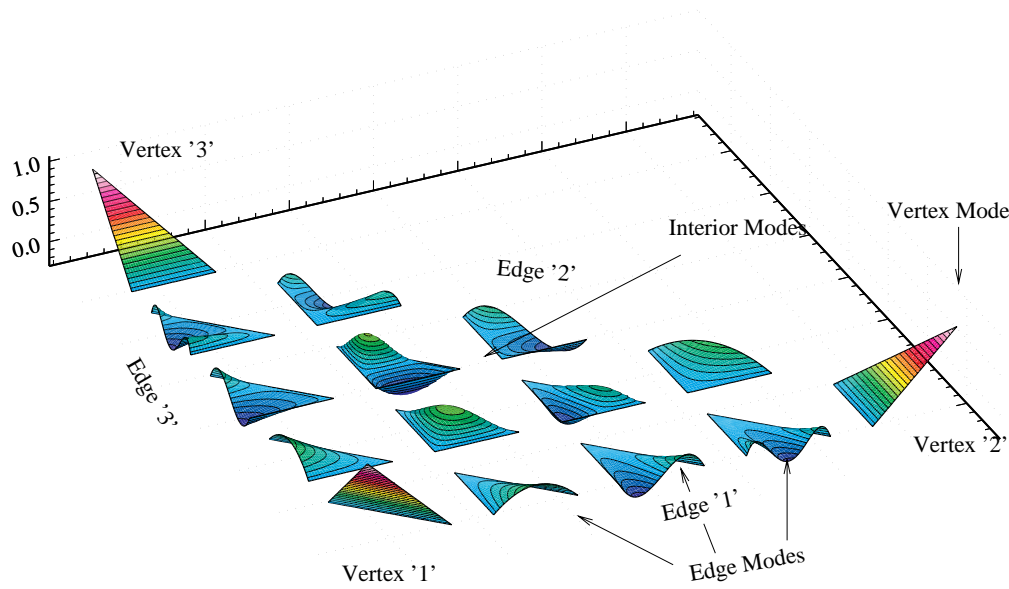
We can ensure that the approximation is continuous over an element-element boundary by making the bases of the triangles continuous there. We need only to make sure that the boundary modes are continuous between elements, since the interior modes are zero on the boundary. We associate a set of modes with an edge. These modes are zero on the other edges and they form a set of one-dimensional shape functions on the edge. We construct the mode set for each edge so that they have the same set of one-dimensional shape functions. This allows us to match the edge shape functions for two elements that share any two of their edges. When two elements share an edge, their respective local coordinates might be running in different directions on the edge; we will deal with this case separately for each of the two bases we define.

To complete the notation we introduce an abbreviated terminology, consisting of three letters, for the five bases we present. The first letter denotes the domain shape (T: triangle, Q: quadrilateral); the second letter denotes the type of basis on the edges (H: hierarchical, N: nonhierarchical); and the third letter denotes the type of the basis in the interior (H: hierarchical, N: nonhierarchical). For example, the first basis function we introduce in the following section is denoted by THH since it is for triangles with hierarchy both in the edge modes and in the interior.

3. Modal basis. A modal basis for triangle elements has been presented in [14] and [16], and it was applied to fluid dynamics problems in [15] and to geophysical fluid dynamics problems in [17]. We now consider a basis for quadrilaterals which is compatible with the triangle basis and thus they can be used together. This combination was first proposed in [18] for a set of three-dimensional polyhedra.

3.1. Triangle basis: THH. We present here a basis which is a set of tensor products in Q^2 and polynomials in T^2 . It maintains numerical linear independence up to high orders due to the construction of the interior modes from Jacobi polynomials with carefully chosen (α, β) coefficients to ensure that mode shapes do not become too similar. Increasing α shifts the roots of the Jacobi polynomials away from the coordinate singularity at $b = 1$ as demonstrated in [16], and hence the modes are prevented from having the same shape at this vertex.

The form of the THH basis is as follows:

FIG. 3. Mode shapes for the triangle modal basis (THH) with $N = 5$.

Vertex modes:

$$\begin{aligned}\phi^{vertex_1} &= \left(\frac{1-a}{2}\right) \left(\frac{1-b}{2}\right), \\ \phi^{vertex_2} &= \left(\frac{1+a}{2}\right) \left(\frac{1-b}{2}\right), \\ \phi^{vertex_3} &= 1. \left(\frac{1+b}{2}\right).\end{aligned}$$

Edge modes ($2 \leq m; 1 \leq n, m < M; m + n < N$):

$$\begin{aligned}\phi_m^{edge_1} &= \left(\frac{1+a}{2}\right) \left(\frac{1-a}{2}\right) P_{m-2}^{1,1}(a) \left(\frac{1-b}{2}\right)^m, \\ \phi_n^{edge_2} &= \left(\frac{1+a}{2}\right) \left(\frac{1-b}{2}\right) \left(\frac{1+b}{2}\right) P_{n-1}^{1,1}(b), \\ \phi_n^{edge_3} &= \left(\frac{1-a}{2}\right) \left(\frac{1-b}{2}\right) \left(\frac{1+b}{2}\right) P_{n-1}^{1,1}(b).\end{aligned}$$

Interior modes ($2 \leq m; 1 \leq n, m < M; m + n < N$):

$$\phi_{mn}^{interior} = \left(\frac{1+a}{2}\right) \left(\frac{1-a}{2}\right) P_{m-2}^{1,1}(a) \left(\frac{1-b}{2}\right)^m \left(\frac{1+b}{2}\right) P_{n-1}^{2m-1,1}(b).$$

Here $P_n^{\alpha,\beta}$ is the n th-order Jacobi polynomial in the $[-1, 1]$ interval with the orthogonality relationship

$$\int_{-1}^1 P_m^{\alpha,\beta}(x) P_n^{\alpha,\beta}(x) (1-x)^\alpha (1+x)^\beta dx = \delta_{mn},$$

where δ_{mn} denotes Kronecker delta. We represent this basis graphically for $N = 5$ in Figure 3; the highest mode is quartic.

3.2. Quadrilateral bases: QHH and QHN. For quadrilateral elements Q^1 is a bijection so we do not need to worry about the coordinate singularity as in the triangle case. We are free to choose a set of modes that are C^0 compatible with the triangle expansion. An obvious choice that guarantees a high degree of orthogonality is the QHH basis:

Vertex modes:

$$\begin{aligned}\phi^{vertex_1} &= \left(\frac{1-a}{2}\right) \left(\frac{1-b}{2}\right), \\ \phi^{vertex_2} &= \left(\frac{1+a}{2}\right) \left(\frac{1-b}{2}\right), \\ \phi^{vertex_3} &= \left(\frac{1+a}{2}\right) \left(\frac{1+b}{2}\right), \\ \phi^{vertex_4} &= \left(\frac{1-a}{2}\right) \left(\frac{1+b}{2}\right).\end{aligned}$$

Edge modes ($2 \leq n, m < N$):

$$\begin{aligned}\phi_m^{edge_1} &= \left(\frac{1+a}{2}\right) \left(\frac{1-a}{2}\right) P_{m-1}^{1,1}(a) \left(\frac{1-b}{2}\right), \\ \phi_n^{edge_2} &= \left(\frac{1+a}{2}\right) \left(\frac{1-b}{2}\right) \left(\frac{1+b}{2}\right) P_{n-1}^{1,1}(b), \\ \phi_m^{edge_3} &= \left(\frac{1+a}{2}\right) \left(\frac{1-a}{2}\right) P_{m-1}^{1,1}(a) \left(\frac{1+b}{2}\right), \\ \phi_n^{edge_4} &= \left(\frac{1-a}{2}\right) \left(\frac{1-b}{2}\right) \left(\frac{1+b}{2}\right) P_{n-1}^{1,1}(b).\end{aligned}$$

Interior modes ($2 \leq m, n < N$):

$$\phi_{mn}^{interior} = \left(\frac{1+a}{2}\right) \left(\frac{1-a}{2}\right) P_{m-1}^{1,1}(a) \left(\frac{1+b}{2}\right) \left(\frac{1-b}{2}\right) P_{n-1}^{1,1}(b).$$

We represent this basis for $N = 5$ in Figure 4.

Alternatively, we could also choose a second set of modes with an even better orthogonality relationship. To this end, we use the Legendre interpolant functions, which we will investigate more thoroughly in the next section. These nodes are used in a collocation manner to maximize the discrete orthogonality of the modes in the interior region. More specifically, the Legendre quadrature points are used as nodal points as well. We also modify the vertex modes and replace the edge modes with tensor products of the one-dimensional modal basis and the Legendre basis. Similarly, we replace the interior modes with tensor products of only the Legendre basis. This means that edge modes from one edge are orthogonal to edge modes from another edge and all the interior modes. The interior modes are mutually orthogonal and hence we can perform inner products and backward transforms in $O(N^2)$ operations. Before we write the basis we need to define an appropriate Lagrange interpolant in terms of the Legendre polynomial $P_n(x) \equiv P_n^{0,0}$ as

$$h_n(r) = -\frac{(1-r^2)P'_N(r)}{N(N+1)P_N(r_n)(r-r_n)},$$

where r_i denotes the location of roots of $(1-r^2)P'_N(r) = 0$ in the interval $[-1, 1]$. Also, by definition we have that $h_n(r_m) = \delta_{mn}$. This construction destroys the hierarchy of

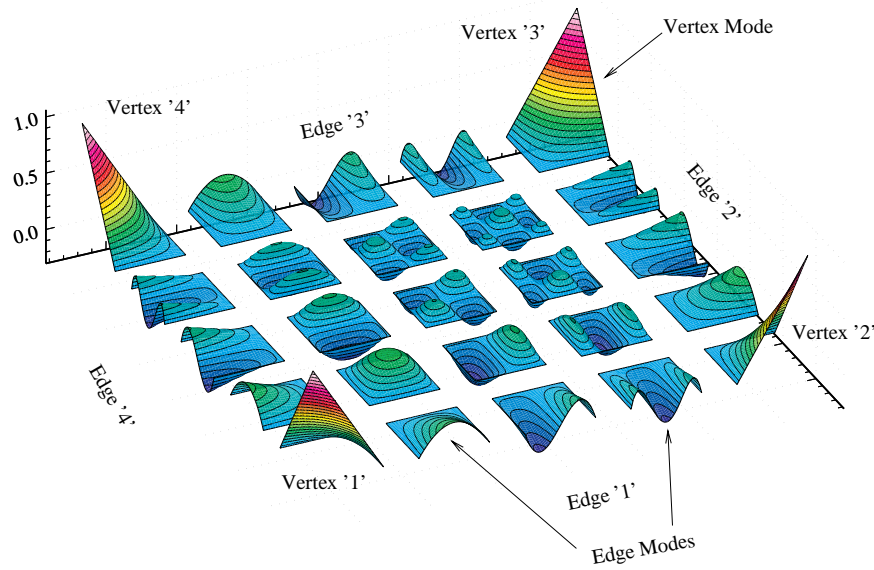


FIG. 4. Mode shapes for the quadrilateral modal basis (QHH) with $N = 5$.

the basis in the interior of the element. More specifically, this QHN basis is defined as follows.

Vertex modes:

$$\begin{aligned}\phi^{vertex_1} &= h_1(a) \left(\frac{1-b}{2} \right) + h_1(b) \left(\frac{1-a}{2} \right) - h_1(a)h_1(b), \\ \phi^{vertex_2} &= h_N(a) \left(\frac{1-b}{2} \right) + h_1(b) \left(\frac{1+a}{2} \right) - h_N(a)h_1(b), \\ \phi^{vertex_3} &= h_N(a) \left(\frac{1+b}{2} \right) + h_N(b) \left(\frac{1+a}{2} \right) - h_N(a)h_N(b), \\ \phi^{vertex_4} &= h_1(a) \left(\frac{1+b}{2} \right) + h_N(b) \left(\frac{1-a}{2} \right) - h_1(a)h_N(b).\end{aligned}$$

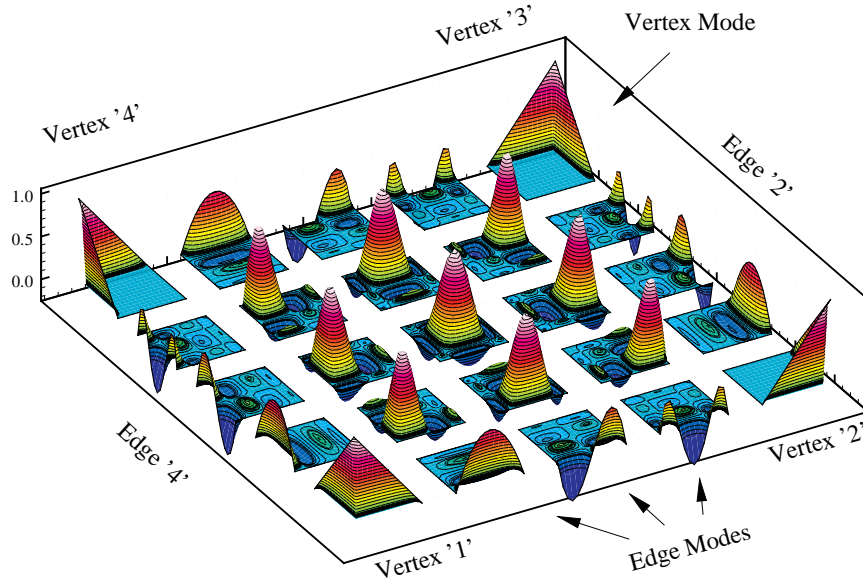
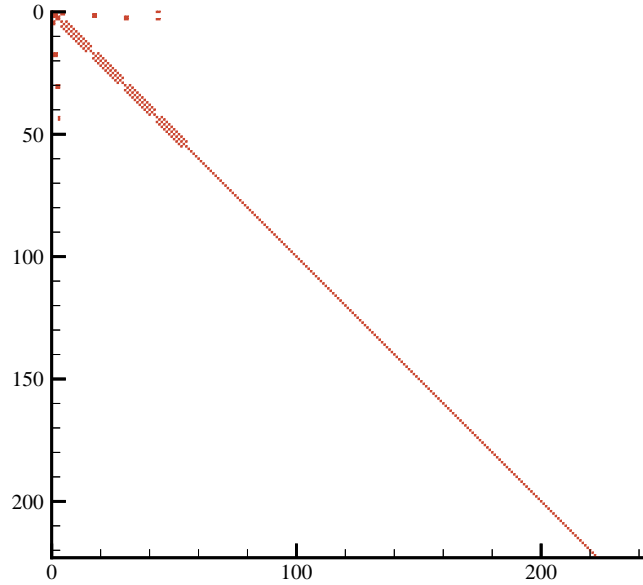
Edge modes ($2 \leq n, m < N$):

$$\begin{aligned}\phi_m^{edge_1} &= \left(\frac{1+a}{2} \right) \left(\frac{1-a}{2} \right) P_{m-1}^{1,1}(a)h_1(b), \\ \phi_n^{edge_2} &= h_N(a) \left(\frac{1-b}{2} \right) \left(\frac{1+b}{2} \right) P_{n-1}^{1,1}(b), \\ \phi_m^{edge_3} &= \left(\frac{1+a}{2} \right) \left(\frac{1-a}{2} \right) P_{m-1}^{1,1}(a)h_N(b), \\ \phi_n^{edge_4} &= h_1(b) \left(\frac{1-b}{2} \right) \left(\frac{1+b}{2} \right) P_{n-1}^{1,1}(b).\end{aligned}$$

Interior modes ($2 \leq m, n < N$):

$$\phi_{mn}^{interior} = h_m(a)h_n(b).$$

Note that according to our convention we have that $h_1(-1) = 1$ and $h_N(1) = 1$, etc. In Figure 5 we see that the edge modes now have behavior localized to the edge,

FIG. 5. Mode shapes for the quadrilateral mixed modal basis with $N = 5$.FIG. 6. Mass matrix for the quadrilateral mixed modal basis (QHN) with $N = 15$.

and the same is true for the vertex modes. In Figure 6 we present graphically the inner product (ϕ_{mn}, ϕ_{pq}) which is the mass matrix for this basis. Here, we order the vertices first (around the origin), followed by the edges and the interior contributions. We verify that indeed there exists great sparsity in this matrix indicative of the strong orthogonality between modes.

4. Mixed nodal-modal basis. We have so far presented a hybrid basis derived from Dubiner's [14] C^0 basis for the triangle. This dictates the shapes of the edge

and vertex modes for the quadrilateral. We will now consider an alternative starting point. In the spectral element method [3], quadrilateral elements are commonly used with a nodal basis, constructed from the Legendre interpolant polynomials. This method benefits from a fast transform to the polynomial space, due to the collocation property of the modes. Similarly, inner products can be evaluated efficiently.

4.1. Quadrilateral basis: QNN. This basis is constructed based on the GLL interpolant of order N already defined as $\{h_n(r)\}$. It was first used for spectral element discretizations in [19]. This is a nodal nonhierarchical basis.

For consistency we present the QNN basis in the same format as the hierarchical basis.

Vertex modes:

$$\begin{aligned}\phi^{vertex_1} &= h_1(a)h_1(b), \\ \phi^{vertex_2} &= h_N(a)h_1(b), \\ \phi^{vertex_3} &= h_N(a)h_N(b), \\ \phi^{vertex_4} &= h_1(a)h_N(b).\end{aligned}$$

Edge modes ($1 < n, m < N$):

$$\begin{aligned}\phi_m^{edge_1} &= h_m(a)h_1(b), \\ \phi_n^{edge_2} &= h_N(a)h_n(b), \\ \phi_m^{edge_3} &= h_m(a)h_N(b), \\ \phi_n^{edge_4} &= h_1(a)h_n(b).\end{aligned}$$

Interior modes ($1 < n, m < N$):

$$\phi_{mn}^{interior} = h_m(a)h_n(b).$$

We represent this basis for $N = 5$ in Figure 7; all modes are fourth-degree polynomials.

4.2. Triangle basis. We will discuss four ways that the triangle basis can be constructed but will eliminate three of them due to undesirable properties of the resulting basis. A first approach might be to construct the triangle basis in the same way as the quadrilateral, using a complete set of N^2 tensor products of the Legendre interpolant functions $\{h_n\}$. However, this basis suffers from overresolution at the singular vertex of the coordinate system as shown in [14]. To avoid this overresolution we could choose a subset of the Legendre interpolant functions on T^2 , as suggested in [20]. However, this leads to a basis that suffers from numerical linear dependency as noted in [14]. Last, we could construct a two-dimensional nodal basis in the manner of [21] or [22] by explicitly specifying the node distribution, but these bases do not have the tensor product property, thus making transforms and inner products expensive $O(N^4)$ operations.

Instead, we propose a basis that is compatible with the nodal quadrilaterals (QNN) and numerically similar to the modal triangle basis (THH). The C^0 continuity condition requires that the boundary modes of the triangle have the same shape as the $\{h_n\}$ modes of the quadrilaterals they can share an edge with. However, this condition does not determine how the modes should be shaped in the interior of the triangle, which leaves us a certain amount of freedom. We insist that the modes are polynomials in (r, s) and that the basis spans the polynomial \mathcal{P}_N . We complete the

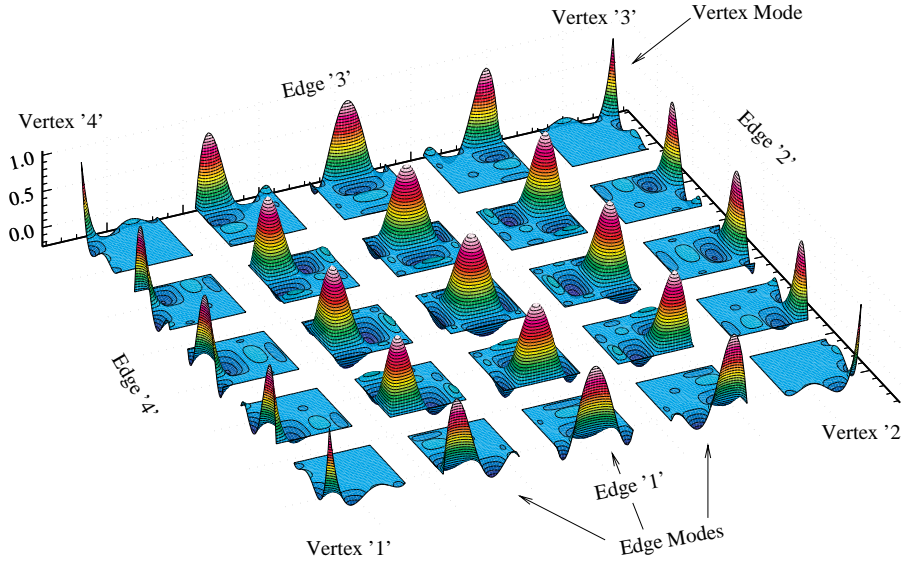


FIG. 7. Mode shapes for the quadrilateral nodal basis (QNN) with $N = 5$.

requirement that the bases be numerically similar by ensuring the new basis is numerically linearly independent. This is guaranteed by using the same interior modes as the modal triangle basis. As previously discussed, the choice of (α, β) for the Jacobi polynomials is key in ensuring that the interior modes do not degenerate in the (r, s) coordinate system but are still tensor products in the (a, b) coordinates.

We constructed the vertex and edge modes of the new basis in the (r, s) coordinates. The vertex 3, edge 2, edge 3, and interior modes still maintain tensor product in the (a, b) coordinates but the remaining boundary modes become two-dimensional functions in this frame. These new modes will increase the constant factor in the asymptotic cost of inner products and transforms compared to the modal triangle.

The new basis is presented in closed form, but we note that it could also be derived as a linear combination of modes from the modal basis, and this is how we guarantee that it will share all properties that the modal basis has for linear operations.

Thus we now present the nodal-compatible TNH basis for the triangle.

In local Cartesian coordinates the following apply:

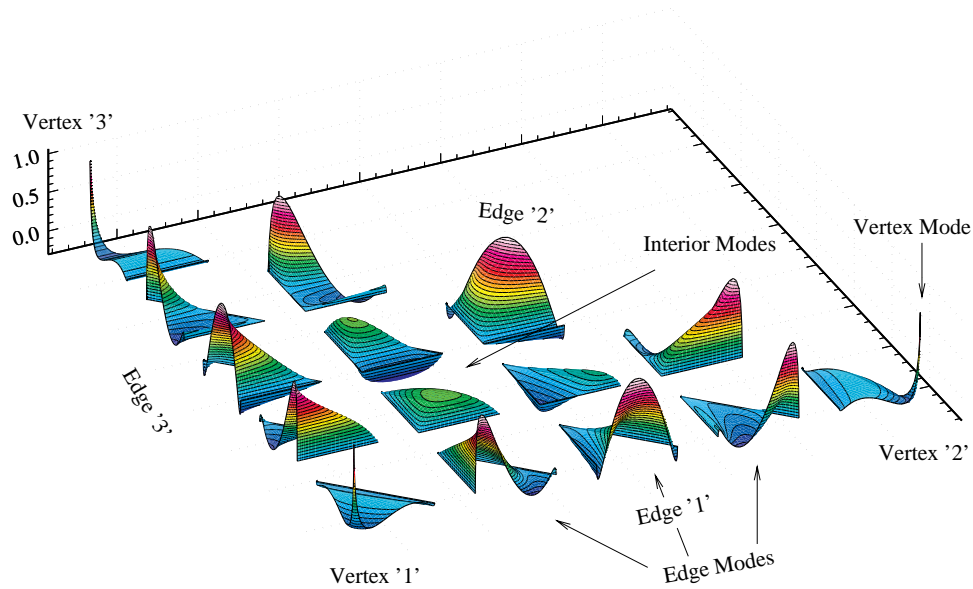
Vertex modes:

$$\begin{aligned}\phi^{vertex_1} &= h_1(r + s + 1), \\ \phi^{vertex_2} &= h_N(r), \\ \phi^{vertex_3} &= h_N(s).\end{aligned}$$

Edge modes ($2 < m, n \leq N$):

$$\begin{aligned}\phi_m^{edge_1} &= -\left(\frac{r+s}{1-r}\right)h_{m-1}(r), \\ \phi_n^{edge_2} &= \left(\frac{1+r}{1-s}\right)h_{n-1}(s), \\ \phi_n^{edge_3} &= -\left(\frac{r+s}{1-s}\right)h_{n-1}(s).\end{aligned}$$

In standard triangular coordinates the following apply:

FIG. 8. Mode shapes for the triangle mixed basis (TNH) with $N = 5$.

Vertex modes:

$$\begin{aligned}\phi^{vertex_1} &= h_1 \left(a \left(\frac{1-b}{2} \right) + \left(\frac{1+b}{2} \right) \right), \\ \phi^{vertex_2} &= h_N \left(a \left(\frac{1-b}{2} \right) - \left(\frac{1+b}{2} \right) \right), \\ \phi^{vertex_3} &= h_N(b).\end{aligned}$$

Edge modes ($2 < m, n < N$):

$$\begin{aligned}\phi_m^{edge_1} &= -\frac{(1-a)(1-b)}{4 - (1+a)(1-b)} h_{m-1} \left(a \left(\frac{1-b}{2} \right) - \left(\frac{1+b}{2} \right) \right), \\ \phi_n^{edge_2} &= \left(\frac{1+a}{2} \right) h_{n-1}(b), \\ \phi_n^{edge_3} &= \left(\frac{1-a}{2} \right) h_{n-1}(b).\end{aligned}$$

The interior modes are unchanged from the modal triangle basis.

We represent this basis for $N = 5$ in Figure 8; the interior modes still have the bubble shape and thus they are zero at the boundaries.

5. Discretization of linear operators. In this section we consider the discretization of the projection, the convection, and the diffusion linear operators. They are formulated as discrete operators in each element and then globally assembled over the entire domain.

5.1. Projection operator. We construct the Galerkin projection that minimizes the L_2 error for approximation of a function by the C^0 basis. First we define the elemental Jacobi transform from the polynomial space to the physical space:

$$u = \sum_{n=0}^N \hat{u}_n \phi_n,$$

where \hat{u}_n is the coefficient of the n th basis function ϕ_n . From this we can obtain an approximation for the coefficients \hat{u}_n . If we take the inner product of both sides with ϕ_m we obtain

$$(\phi_m, u) = \sum^N (\phi_m, \phi_n) \hat{u}_n,$$

which we can solve for \hat{u}_n since (ϕ_m, ϕ_n) is positive definite [15]. Explicitly, we can write the projection coefficients as

$$\hat{u}_m = B_{mn}^{-1}(\phi_n, u),$$

where B is the matrix with entries $B_{mn} = (\phi_m, \phi_n)$. This approximation minimizes the residual

$$r = \|u - \sum^N \hat{u}_m \phi_m\|_{L_2}.$$

We can now construct a matrix transform between the modal basis and the mixed basis. Since each ϕ^{mixed} is a polynomial of degree $N - 1$, we can approximate it (to machine precision) by a linear combination of modes in terms of the modal basis by using the Jacobi transform

$$\phi_m^{mixed} = A_{mn} \phi_n^{modal},$$

where

$$A_{mn} = B_{mi}^{-1}(\phi_i^{modal}, \phi_n^{mixed})$$

and here $B_{mn} = (\phi_m^{modal}, \phi_n^{modal})$.

Let us consider the residual r^{mixed} for approximation of a function u by the mixed basis and the associated coefficients \hat{u}_m . Clearly, we can see that this must also be the residual for the modal basis since

$$r^{mixed} = \left\| u - \sum^N \hat{u}_m \phi_m^{mixed} \right\|_{L_2} = \left\| u - \sum^N \sum^N A_{mn} \hat{u}_m \phi_n^{modal} \right\|_{L_2}.$$

Hence, we expect the approximation residual to be the same in the L_2 norm. Next we will examine the behavior of the elemental projection operator and describe how well the bases approximate functions in the L_2 norm.

5.1.1. Convergence in skew elements. We now consider the effect of the T^1 and Q^1 mappings on the accuracy of the projection operator. In Figure 9 we examine eight different meshes consisting of triangles and quadrilaterals. We start by projecting $\sin(\pi x) \sin(\pi y)$ onto a square domain covered with standard elements. We see in Figures 10 and 11, which show results for the *modal* and *mixed* bases, respectively, that exponential convergence is achieved. Subsequently, we make the elements covering the domain progressively more skewed in the meshes B–H. In each case we see that exponential convergence is achieved, even when one of the triangular elements has a minimum angle of about 10^{-3} degrees. This shows that the accuracy of the method is extremely robust to badly shaped elements. Also, we note that the similarity of the convergence curves demonstrates that the rate of exponential convergence is unaffected by the skewing.

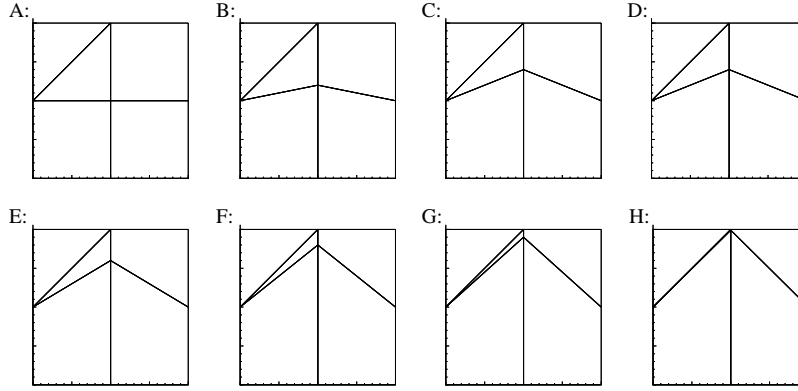


FIG. 9. Meshes (A–H) consist of three quadrilaterals and two triangles which are progressively skewed by shifting the interior vertex.

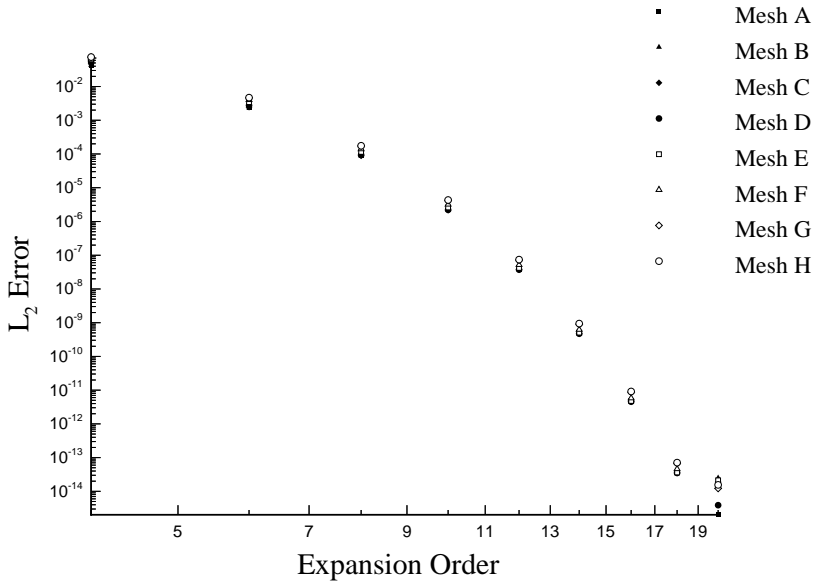


FIG. 10. Convergence in the L_2 norm for modal projection of the function $u = \sin(\pi x) \sin(\pi y)$ on meshes A–H.

5.2. Convective operator. We now consider the two-dimensional linear advection equation with coefficients $(\cos(\theta), \sin(\theta))$ for $u(x, y; t)$:

$$\frac{\partial u(x, y; t)}{\partial t} + Lu \equiv \frac{\partial u}{\partial t} + \cos(\theta) \frac{\partial u}{\partial x} + \sin(\theta) \frac{\partial u}{\partial y} = 0.$$

This has been formulated for triangular elements in [15], and we note that using quadrilateral elements requires very few changes to this method. We consider the weak form of this equation in Ω^k as follows.

Find $u \in H^1(\Omega)$ such that $\forall w \in H^1(\Omega)$

$$\left(\frac{\partial u}{\partial t} - \cos(\theta) \cdot \frac{\partial u}{\partial x} - \sin(\theta) \cdot \frac{\partial u}{\partial y}, w \right) = 0 \quad \forall w \in H^1(\Omega).$$

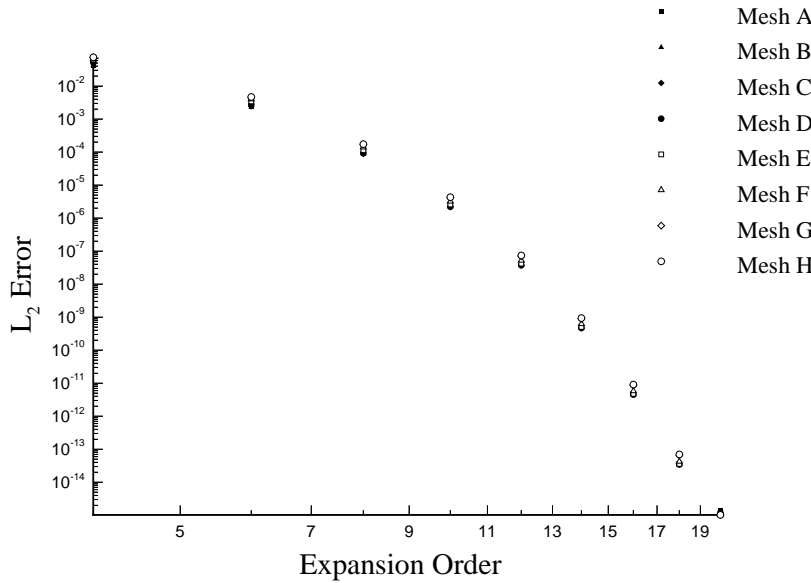


FIG. 11. Convergence in the L_2 norm for mixed projection of the function $u = \sin(\pi x) \sin(\pi y)$ on meshes A–H.

Following a Galerkin formulation so that the trial and test spaces are spanned by the same basis we obtain

$$(\phi_n, \phi_m) \frac{d\hat{u}_m}{dt} = \left[\left(\phi_n, \cos(\theta) \frac{\partial \phi_m}{\partial x} \right) + \left(\phi_n, \sin(\theta) \frac{\partial \phi_m}{\partial y} \right) \right] \hat{u}_m.$$

We now define two local operators B_k and $L_k(\theta)$:

$$B_k = (\phi_n^k, \phi_m^k),$$

$$L_k(\theta) = \left[\cos(\theta) \left(\phi_n^k, \frac{\partial \phi_m^k}{\partial x} \right) + \sin(\theta) \left(\phi_n^k, \frac{\partial \phi_m^k}{\partial y} \right) \right].$$

Based on these definitions we now construct two new operators for the entire domain:

$$L(\theta) = \begin{bmatrix} L_1 & 0 & \dots & 0 \\ 0 & L_2 & \dots & 0 \\ \dots & \dots & \dots & \dots \\ 0 & 0 & \dots & L_K \end{bmatrix}$$

and similarly

$$B = \begin{bmatrix} B_1 & 0 & \dots & 0 \\ 0 & B_2 & \dots & 0 \\ \dots & \dots & \dots & \dots \\ 0 & 0 & \dots & B_K \end{bmatrix}.$$

We can now assemble these elemental operators into a global operator by means of the Z operator that assembles the local coefficients into the global coefficients and ensures C^0 continuity.

To illustrate this global assembly procedure, we consider a global domain made up of two elements as shown in Figure 12. The expansion order shown here is $N = 3$,

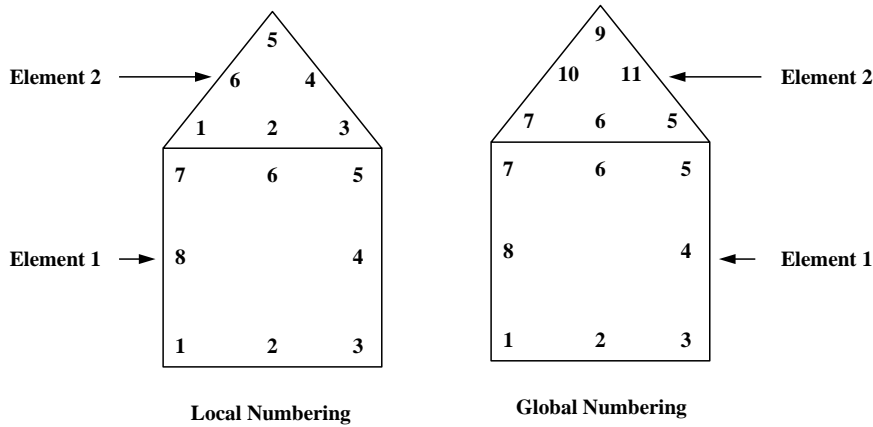


FIG. 12. Illustration of local and global numbering for a domain containing one quadrilateral and one triangular element. Here the expansion order is $N = 3$, and we show only the boundary modes.

which means there are six boundary modes on the triangle and eight boundary modes on the quadrilateral.

The total number of local degrees of freedom is therefore $N_{local} = 14$. Since three modes meet along the connecting edge the number of global degrees of freedom is 11 and so for this case Z is a 14×11 matrix:

$$\hat{u}_l = \begin{bmatrix} \hat{u}_1^1 \\ \hat{u}_2^1 \\ \hat{u}_3^1 \\ \hat{u}_4^1 \\ \hat{u}_5^1 \\ \hat{u}_6^1 \\ \hat{u}_7^1 \\ \hat{u}_8^1 \\ \dots \\ \hat{u}_1^2 \\ \hat{u}_2^2 \\ \hat{u}_3^2 \\ \hat{u}_4^2 \\ \hat{u}_5^2 \\ \hat{u}_6^2 \end{bmatrix} = \begin{bmatrix} 1 & & & & & & & & & & \\ & 1 & & & & & & & & & \\ & & 1 & & & & & & & & \\ & & & 1 & & & & & & & \\ & & & & 1 & & & & & & \\ & & & & & 1 & & & & & \\ & & & & & & 1 & & & & \\ & & & & & & & 1 & & & \\ & & & & & & & & 1 & & \\ & & & & & & & & & 1 & \\ & & & & & & & & & & 1 \\ & & & & & & & & & & & 1 \end{bmatrix} \begin{bmatrix} \hat{u}_1^g \\ \hat{u}_2^g \\ \hat{u}_3^g \\ \hat{u}_4^g \\ \hat{u}_5^g \\ \hat{u}_6^g \\ \hat{u}_7^g \\ \hat{u}_8^g \\ \hat{u}_9^g \\ \hat{u}_{10}^g \\ \hat{u}_{11}^g \end{bmatrix}.$$

The superscripts denote the local or global nodal number and the subscripts denote the element number. The absolute column sum gives the multiplicity of a mode and we see that columns 5, 6, and 7 all have a multiplicity of 2. We also note that the absolute row sum is always 1 since there is ever only one value of each local mode. It is also possible to have a (-1) entry if we have two elements where (1) edge 1 meets edge 1, (2) edge 1 meets edge 2, (3) edge 2 meets edge 2, (4) edge 3 meets edge 3, (5) edge 3 meets edge 4, or (6) edge 4 meets edge 4; then the local coordinates at the edges are in opposite directions. If we are using a hierarchical basis, then we need to negate odd modes along one of the edges.

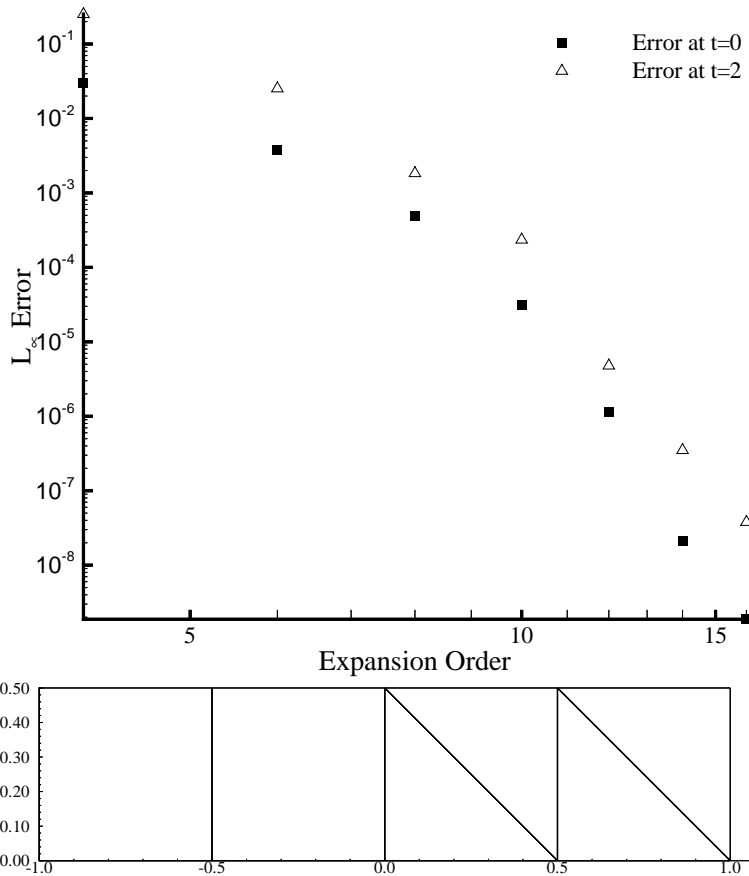


FIG. 13. Exponential accuracy is achieved for the wave equation with $u = \sin(\pi \cos(\pi x))$ as initial condition.

Having defined the assembly operation, we can now write the global system as

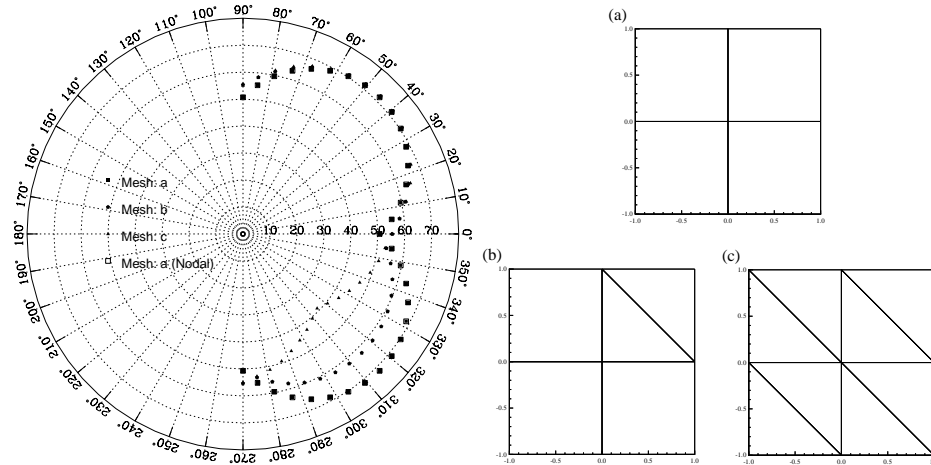
$$\frac{d\hat{\mathbf{u}}^g}{dt} = G(\theta)\hat{\mathbf{u}}^g,$$

where $G(\theta) = (Z^t B Z)^{-1} (Z^t L(\theta) Z)$.

The behavior of this operator is very important for determining the maximum time step we will be able to use for any problem which involves an explicit treatment of advection contributions.

5.2.1. Accuracy of the convective operator. We tested the accuracy of the Galerkin convective operator using a third-order Adams–Bashforth temporal scheme and a periodic domain as shown in Figure 13. We started with initial condition $u = \sin(\pi \cos(\pi x))$ and examined the initial projection L_∞ error and again at $t = 2$. The convection velocity was constant. We chose a time step small enough so that the time stepping error is small compared to the initial projection error for $N < 16$. We see that exponential convergence is maintained after one time period.

5.2.2. Spectrum of the convective operator. We can now examine the behavior of this operator by examining its eigenspectrum. The distribution of the spectral radius, $\rho(\theta)$, shows us the level of directional inhomogeneity of wave speed sup-

FIG. 14. Spectral radius of the weak convective operator on a periodic domain, $N = 12$.

ported in a given domain. We first consider a periodic box that is discretized with essentially standard elements, and then we examine how deforming these elements within the box affects wave propagation.

In Figure 14 we show three discretizations of the periodic box; (a) employs only quadrilaterals, (b) a mix of quadrilaterals and triangles, and (c) only triangles. $G(\theta)$ was constructed using a 12th-order expansion and the spectral radius of the $G(\theta)$ for each mesh is shown as a function of θ . In the upper right quadrant we see that the spectral radii are very similar for all three cases, but in the lower right quadrant we see that there is a marked difference between the spectral radii of the quadrilateral mesh and the triangle mesh with the hybrid mesh between these two cases.

Theoretically, we do not have to consider the spectral radius of the mixed basis, as we have shown that since it is numerically similar to the modal basis it will share the same spectral properties for linear operators. However, we did run this test for the quadrilaterals using a nodal basis and obtained the same spectral radius to machine precision, confirming the theory. Hence the symbols for the nodal quadrilateral mesh and the modal quadrilateral mesh are identical.

So far we have examined the spatial variation at a given expansion order. In Figure 15 we now demonstrate that $\sup_{\theta} \rho(G(\theta))$ grows as $O(N^2)$ for the modal basis used on all three meshes, and again we note that the mixed basis has exactly the same property to machine precision.

We have an *exact* fit for the numerical spectral envelope of the Galerkin convective operator on a periodic square domain discretized with regular quadrilaterals. This can be represented as (see also Figure 16)

$$\rho_{\square}(\theta) = \begin{cases} \sqrt{2}\rho_{\square}(0) \sin(\theta + \frac{\pi}{4}) & \text{if } \theta > 0, \\ \sqrt{2}\rho_{\square}(0) \sin(\theta + \frac{3\pi}{4}) & \text{otherwise.} \end{cases}$$

We can motivate this result by noticing that the mesh and operator are both aligned to the (x, y) directions. Thus we can look for polynomial solutions to the eigenvalue equation in each one dimension, given a set of one-dimensional discrete solutions to

$$\left(\phi_n^k, \frac{\partial \phi_m^k}{\partial x} \right) c_m = \lambda_{1d} (\phi_n^k, \phi_m^k).$$

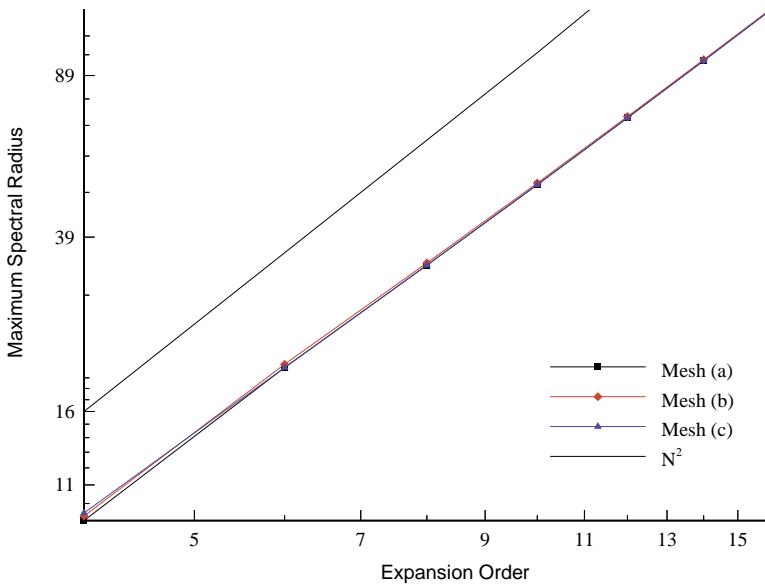


FIG. 15. Growth of the spectral radius of the Galerkin convective operator with expansion order.

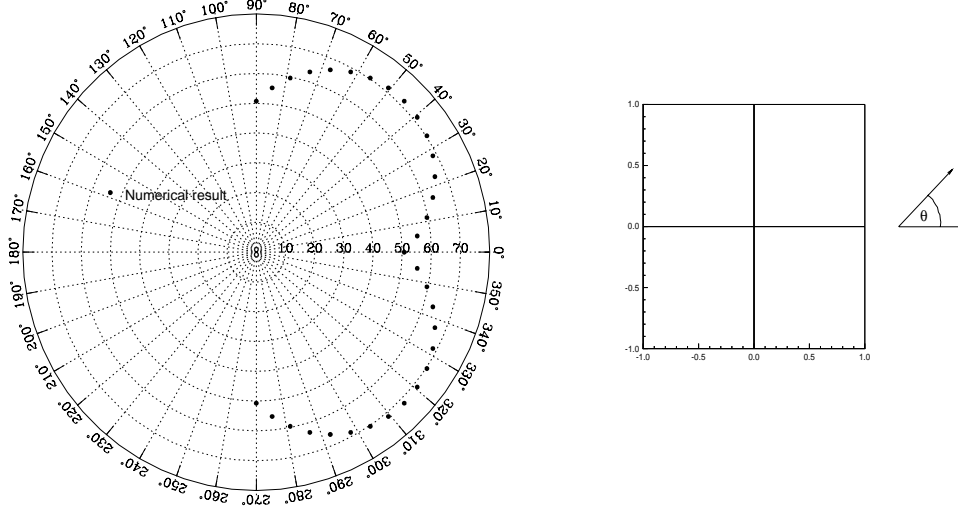


FIG. 16. $\rho_{\square}(\theta)$ is an exact fit for the spectral radius of the Galerkin convective operator on a periodic domain tiled with regular quadrilaterals and with $N = 12$.

Additionally we require that the solution be periodic over every subdomain. Next we make a tensor product of the discrete eigenfunction that has the largest eigenvalue (f_{max}). This function $f_{max}(x)f_{max}(y)$ is an eigenfunction of the full two-dimensional equation and has eigenvalue $\lambda_{1d}(\cos(\theta) + \sin(\theta))$ for $\theta \in (0, \frac{\pi}{2})$.

We also have an approximate fit for the numerical spectral envelope of the Galerkin convective operator on a periodic square domain discretized with regular triangles. This is described by (see also Figure 17)

$$\rho_{\triangle}(\theta) \approx \begin{cases} \sqrt{2} \left(\rho_{\triangle}(0) \sin(\theta + \frac{\pi}{4}) - \frac{\rho_{\triangle}(0)}{2} \sin(2\theta) \right) & \text{if } \theta > 0, \\ \sqrt{2}(\rho_{\triangle}(0) \sin(\theta + \frac{3\pi}{4}) + (\rho_{\triangle}(0) - \rho_{\square}(0)) \sin(2\theta)) & \text{otherwise.} \end{cases}$$

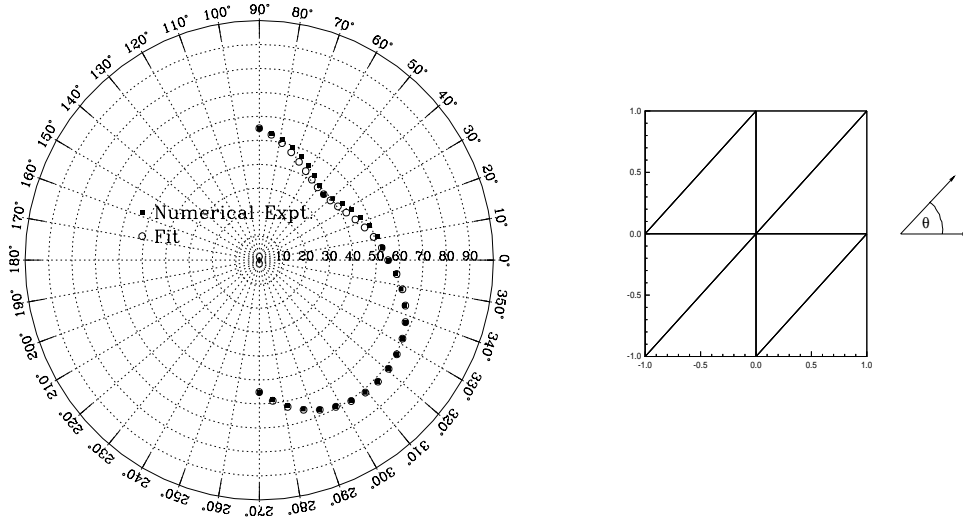


FIG. 17. $\rho_{\Delta}(\theta)$ is a close fit for the spectral radius of the Galerkin convective operator on a periodic domain tiled with triangles and with $N = 12$.

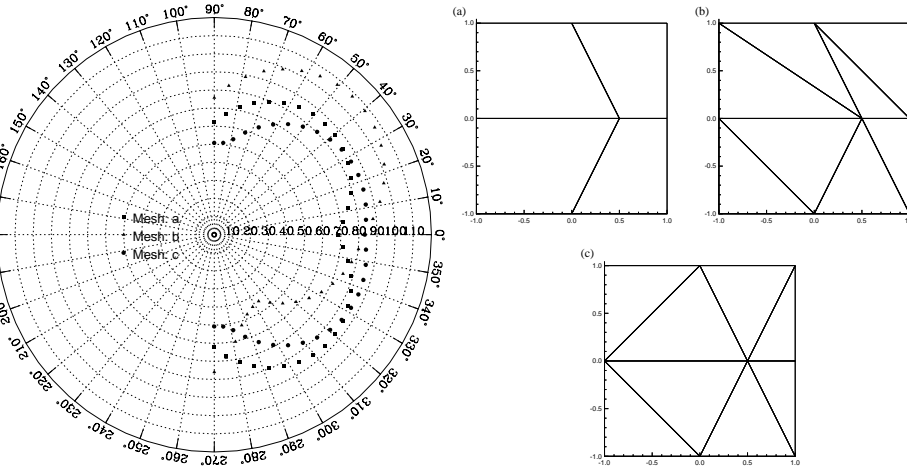


FIG. 18. Spectral radius of the Galerkin convective operator on a periodic domain discretized with nonregular elements.

So far we have not indicated how the operator $G(\theta)$ depends on the mappings T^1 and Q^1 . We will now consider the same periodic box discretized with deformed elements so that these mappings are not simply scaled identities. In Figure 18 we have created deformed elements by simply shifting the vertex in the middle of the quadrilateral and triangle meshes we have just considered. In addition, we created a new triangle mesh by taking the Delaunay triangulation of the given vertices. This time we see that the deformation of the triangle mesh has increased the spectral inhomogeneity of the operator but that this can be ameliorated by choosing the Delaunay triangulation.

5.3. Diffusion operator. We now consider the two-dimensional elliptic Helmholtz equation

$$(\nabla^2 - \lambda) u = f, \quad \lambda > 0.$$

Again using the Galerkin formulation and integrating by parts we obtain

$$[(\nabla \phi_m, \nabla \phi_n) + \lambda (\phi_m, \phi_n)] \hat{u}_n = (\phi_m, f) + \int_{\partial\Omega} \phi_m \frac{\partial u}{\partial n} ds.$$

We will define a new set of K operators

$$L_k = [(\nabla \phi_m^k, \nabla \phi_n^k) + \lambda (\phi_m, \phi_n)]$$

and a new set of K vectors

$$F_k = (\phi_m, f) + \int_{\partial\Omega^k} \phi_m \frac{\partial u}{\partial n} ds.$$

Then repeating the process to assemble the weak convective operator we can assemble the subdomain operators into a global operation to obtain

$$\hat{\mathbf{u}}^g = (Z^t L Z)^{-1} Z^t \mathbf{F},$$

where the bold letters denote vectors.

5.3.1. Convergence. The above system was solved directly using the Schur complement method approach outlined in [15].

In Figure 19 we demonstrate convergence to the exact solution with p -refinement and h -refinement for the Helmholtz equation with $\lambda = 1$ for Dirichlet boundary conditions.

In Figure 20 we show p -type convergence for a more complicated exact solution. This example demonstrates that the method is stable to at least $N = 64$.

6. Comparison of the bases. We have presented two classes of bases in sections 3 and 4 that give the same approximations and share the same spectral properties. We are left with the decision of which basis we should use for a given problem. In this section we summarize their properties and suggest possible selection criteria.

First, we consider the structure of the mass and stiffness matrix encountered in the convection and diffusion equations, respectively. We concentrate on the triangular elements only, and we examine the different structures corresponding to bases THH and TNH. The elemental mass matrix is the matrix which has entries defined by

$$B_{mn} = (\phi_m, \phi_n).$$

Figure 21 shows (a) the mass matrix for the THH basis and (b) the mass matrix for TNH. We also include in Figure 21(c) the mass matrix corresponding to TNH but resulting from performing an exact integration. In the latter case the number of quadrature points needed is larger than the nodal points, unlike the case in (b) where the quadrature points coincide with the nodes at the edges. We notice that the sparsity of the mass matrices corresponding to bases represented in (b) and (c) is reduced compared to the THH modal basis, but this is to be expected because each boundary mode in TNH is a linear combination of all of the THH boundary modes.

We can also compare the elemental stiffness matrix for the THH modal basis and the TNH mixed basis. The stiffness matrix is the matrix which has entries defined by

$$M_{mn} = (\nabla \phi_m, \nabla \phi_n).$$

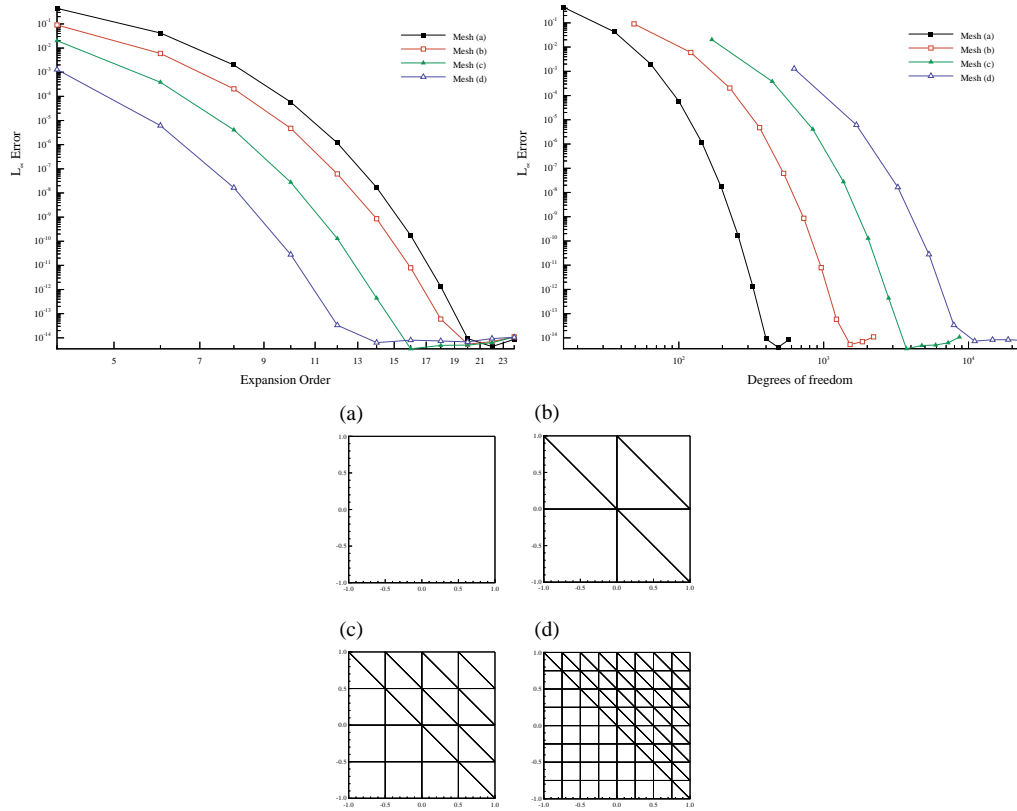


FIG. 19. Convergence test for the Helmholtz equation using quadrilaterals and triangles, with Dirichlet boundary conditions. The exact solution is $u = \sin(\pi x)\cos(\pi y)$ and forcing function $f = -(\lambda + 2\pi^2)\sin(\pi x)\cos(\pi y)$.

Figure 22 shows the two stiffness matrices for $N = 15$. Again the matrix corresponding to TNH basis has a denser structure.

We now summarize the properties of the two classes of bases. The modal basis (THH/QHH) properties are as follows:

- The basis is hierarchical.
- We are able to vary locally the number of modes per edge or interior.
- Elemental transforms and inner products are $O(N^3)$ operations.
- The interior-interior mass matrix is banded.
- The interior-interior stiffness matrix is banded.

In addition, this basis can be enhanced with other properties by varying the form of Jacobi polynomials. For example, an interesting version proposed in [14, 17] uses $(\alpha, \beta) = (2, 2)$ and $(2m+3, 3)$ for the Jacobi constants. It has the following properties:

- The interior-interior mass matrix is diagonal.
- The interior-interior stiffness matrix is full.

There are many different choices in choosing a mixed basis. Their main properties are as follows:

- The basis is nonhierarchical (QHN, TNH, and QNN).
- Gaussian integration order is dictated by the basis order (QNN, TNH at the edges, and QHN in the interior).

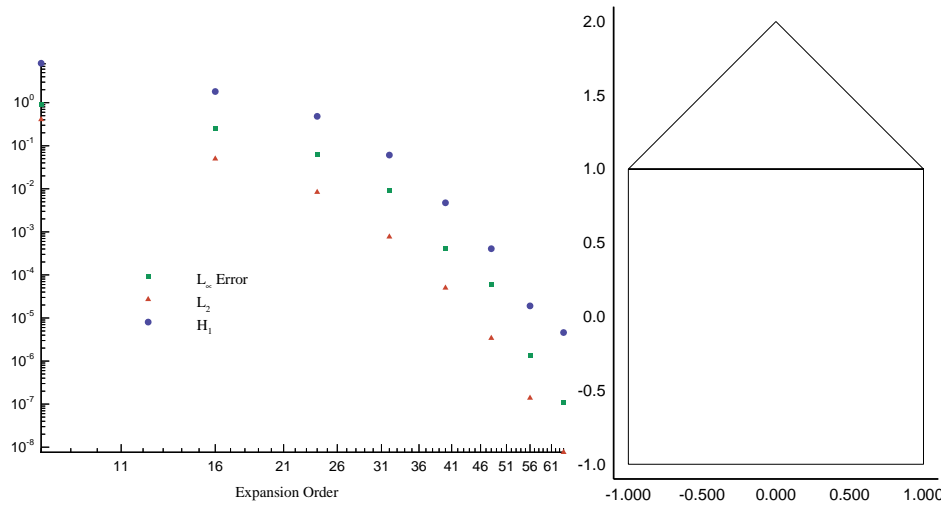


FIG. 20. Convergence test for the Helmholtz, using triangles, with Dirichlet boundary conditions. The exact solution is $u = \sin(\pi \cos(\pi r^2))$ and forcing function $f = -(\lambda + 4\pi^4 r^2 \sin(\pi r^2)^2) \sin(\pi \cos(\pi r^2)) - 4\pi^2(\pi r^2 \cos(\pi r^2) + \sin(\pi r^2)) \cos(\pi \cos(\pi r^2))$, where $r^2 = x^2 + y^2$.

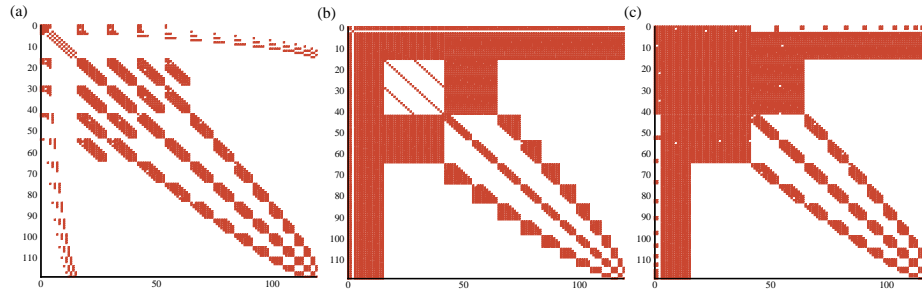


FIG. 21. Comparison of the elemental mass matrix for (a) THH, (b) TNH (collocation), and (c) TNH (exact integration) for $N = 15$.

- The expansion order is (practically) fixed in nodal quadrilaterals (QNN).
- Quadrilateral transforms and inner products cost $O(N^2)$ operations for QNN and $O(4N^2)$ for QHN.
- Triangle transforms and inner products are $O(2N^3)$ operations (TNH).
- The interior-interior mass matrix is banded (TNH); it is extremely sparse for QHN and diagonal for QNN.
- The interior-interior stiffness matrix is banded only for TNH; otherwise it is full.

These properties suggest situations in which each type of basis is appropriate. For example, the modal basis can lead to high computational efficiencies if the following apply:

- The solution has local regions of interesting behavior.
- The solution benefits from nonsteady regions of interesting behavior; this can be captured by local p -refinement.
- The domain is highly irregular and needs a high ratio of triangles to quadrilaterals.

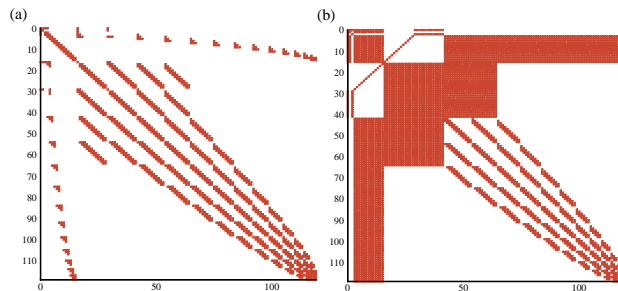


FIG. 22. Comparison of the elemental stiffness matrix for (a) THH and (b) TNH bases for $N = 15$.

On the other hand, the mixed basis can also lead to high efficiencies if the following apply:

- The solution has a uniform variability.
- The domain is locally irregular, and thus it does not require a large number of triangles to complement the quadrilaterals.

More important, it is the specific application that we consider and the dynamic refinement procedure that ultimately decide what basis function is the best choice. In a follow-up paper we show such applications in simulations of incompressible flows in complex geometry domains. If it becomes apparent that an initial choice of basis becomes inappropriate, it is not an expensive operation to transform between bases. In three dimensions there are many more choices as many polymorphic domains are possible, including hexahedra, tetrahedra, prisms, and pyramids. We will report on suitable basis functions for these elements in a future paper.

REFERENCES

- [1] I. BABUSKA, B. A. SZABO, AND I. N. KATZ, *The p-version of the finite element method*, SIAM J. Numer. Anal., 18 (1981), pp. 515–595.
- [2] I. BABUSKA AND M. R. DORR, *Error estimates for the combined h and p-version of the finite element method*, Numer. Math., 37 (1981), pp. 257.
- [3] A. T. PATERA, *A spectral method for fluid dynamics: Laminar flow in a channel expansion*, J. Comput. Phys., 54 (1984), pp. 468.
- [4] G. E. KARNIADAKIS, E. T. BULLISTER, AND A. T. PATERA, *A spectral element method for solution of two- and three-dimensional time dependent Navier-Stokes equations*, in Finite Element Methods for Nonlinear Problems, Springer-Verlag, Berlin, 1985, p. 803.
- [5] J. T. ODEN, A. PATRA, AND Y. FENG, *An hp adaptive strategy*, in AMD 157, Adaptive, Multilevel and Hierarchical Computational Strategies, ASME, 1992.
- [6] L. DEMKOWICZ, J. T. ODEN, AND W. RACHOWICZ, *A new finite element method for solving compressible Navier-Stokes equations based on an operator splitting method and h-p adaptivity*, Comput. Methods Appl. Mech. Engrg., 84 (1990), p. 275.
- [7] J. T. ODEN, T. LISZKA, AND W. WU, *An h-p adaptive finite element method for incompressible viscous flows*, in The Mathematics of Finite Elements and Applications, VII, 13, Academic Press, London, UK, 1991, pp. 13–54.
- [8] C. BERNARDI, Y. MADAY, AND A. T. PATERA, *A new nonconforming approach to domain decomposition: The mortar element method*, in Nonlinear Partial Differential Equations and Their Applications, Pitman Res. Notes Math. Ser. 299, Longman, Harlow, UK, 1994.
- [9] R. BISWAS, K. DEVINE, AND J. FLAHERTY, *Parallel, adaptive finite element methods for conservation laws*, Appl. Numer. Math., 14 (1994), pp. 255–283.
- [10] R. D. HENDERSON AND G. E. KARNIADAKIS, *Unstructured spectral element methods for simulation of turbulence flows*, J. Comput. Phys., 122 (1995), p. 191.
- [11] B. A. SZABO AND I. BABUSKA, *Finite Element Analysis*, John Wiley & Sons, Inc., New York, 1991.

- [12] O. C. ZIENKIEWICZ AND R. L. TAYLOR, *The Finite Element Method*, Vol. 1, McGraw-Hill, New York, 1989.
- [13] A. PEANO, *Hierarchies of conforming finite elements for plane elasticity and plate bending*, Comput. Math. Appl., 2 (1976), p. 221.
- [14] M. DUBINER, *Spectral methods on triangles and other domains*, J. Sci. Comput., 6 (1991), p. 345.
- [15] S. J. SHERWIN AND G. E. KARNIADAKIS, *A triangular spectral method: Applications to the incompressible Navier-Stokes equation*, Comput. Methods Appl. Mech. Engrg., 123 (1995), p. 189.
- [16] S. J. SHERWIN AND G. E. KARNIADAKIS, *A new triangular and tetrahedral basis for high-order finite element methods*, Internat. J. Numer. Methods Engrg., 38 (1995), p. 3775.
- [17] B. A. WINGATE AND J. P. BOYD, *Triangular spectral element methods for geophysical fluid dynamics applications*, in ICOSAHOM'95, Houston, TX, 1995.
- [18] S. J. SHERWIN, *Hierarchical hp finite elements in hybrid domains*, in Finite Elements in Analysis and Design, Vol. 27, Elsevier, New York, 1997, pp. 109–119.
- [19] E. M. RÖNQUIST, *Optimal Spectral Element Methods for the Unsteady Three-Dimensional Incompressible Navier-Stokes Equations*, Ph.D. thesis, Massachusetts Institute of Technology, Cambridge, MA, 1988.
- [20] C. MAVRIPLIS AND J. VAN ROSENDALE, *Triangular Spectral Elements for Incompressible Flow*, AIAA-93-3346, American Institute of Aeronautics and Astronautics, Washington, DC, 1993.
- [21] Q. CHEN AND I. BABUSKA, *Approximate optimal points for the polynomial interpolation of real functions in an interval and in a triangle*, Comput. Methods Appl. Mech. Engrg., 128 (1995), p. 405.
- [22] J. S. HESTHAVEN, *From electrostatics to almost optimal nodal sets for polynomial interpolation in a simplex*, SIAM J. Numer. Anal., 35 (1998), pp. 655–676.